Magnetic imaging of spin waves and magnetic phase transitions with nitrogen-vacancy centers in diamond

Bertelli, I.

4

MAGNETIC RESONANCE IMAGING OF SPIN-WAVE TRANSPORT AND INTERFERENCE IN A MAGNETIC INSULATOR

Spin waves — the elementary excitations of magnetic materials — are prime candidate signal carriers for low-dissipation information processing. Being able to image coherent spin-wave transport is crucial for developing interference-based spin-wave devices. We introduce magnetic resonance imaging of the microwave magnetic stray fields that are generated by spin waves as a new approach for imaging coherent spin-wave transport. We realize this approach using a dense layer of electronic sensor spins in a diamond chip, which combines the ability to detect small magnetic fields with a sensitivity to their polarization. Focusing on a thin-film magnetic insulator, we quantify spin-wave amplitudes, visualize spin-wave dispersion and interference, and demonstrate time-domain measurements of spin-wave packets. We theoretically explain the observed anisotropic spin-wave patterns in terms of chiral spin-wave excitation and stray-field coupling to the sensor spins. Our results pave the way for probing spin waves in atomically thin magnets, even when embedded between opaque materials.

This chapter has been published in *Science Advances* **6**, eabd3556 (2020) by **I. Bertelli**, J. J. Carmiggelt, T. Yu, B. G. Simon, C. C. Pothoven, G. E. W. Bauer, Y. M. Blanter, J. Aarts, T. van der Sar.

4.1. INTRODUCTION

Over the last few decades, the desire to understand and control spin transport, and to use it in information technology, has invigorated the field of spintronics. A central goal of the field is to provide information processing based on the spin of the electron instead of its charge and thereby avoid the heating associated with charge currents. As heating is currently the main obstacle for increasing computational speed, spin-based information processing may provide the next transformative change in information technology.

Promising signal carriers for low-dissipation information transport are spin waves [1, 2] — the collective spin excitations of magnetic materials. Spin waves exist even in electrically insulating magnets, where they are able to propagate inherently free of the dissipative motion of charge. They can have nanometer wavelengths and gigahertz frequencies well suited for chip-scale device technologies and interference-based spin-wave logic circuits [2]. Consequently, a growing research field focuses on spin-wave devices such as interconnects, interferometers, transistors, amplifiers, and spin-torque oscillators [3–7].

Being able to image coherent spin waves in thin-film magnets is crucial for developing spin-wave device technology. Leading techniques for imaging coherent spin waves, such as transmission x-ray microscopy [8, 9], Brillouin light scattering [10], and Kerr microscopy [11], rely on a spin-dependent optical response of a magnetic material. Here, we introduce a new approach: phase-sensitive magnetic resonance imaging of the microwave magnetic stray fields generated by coherent spin waves. We realize this approach using a layer of electronic sensor spins in a diamond chip as imaging platform (Fig. 4.1A). These spins enable quantitative measurements of microwave magnetic fields including their polarization, making the approach well suited for spin-wave imaging in magnetic thin films.

Focusing on a ~200-nm-thick magnetic insulator, we quantify spin-wave amplitudes, visualize the spin-wave dispersion, and demonstrate time-domain measurements of spin-wave packets. We observe unidirectional emission of spin waves that autofocus, interfere, and produce chiral magnetic stray fields with a handedness that matches that of the natural precession of the sensor spins. We present a theoretical analysis of the chiral spin-wave excitation and stray-field coupling to the sensor spins and show that it accurately describes the observed spatial spin-wave maps.

We detect the magnetic fields generated by spin waves using electron spins associated with nitrogen-vacancy (NV) lattice defects in diamond [12]. These spins can be initialized and read out optically and manipulated with high fidelity by microwaves. Over the last decade, NV magnetometry has emerged as a powerful platform for probing static and dynamic magnetic phenomena in condensed matter systems [13]. Key is an NV-sample distance tunable between 10 and 1000 nm that is well matched with the length scales of spin textures such as magnetic domain walls, cycloids, vortices, and skyrmions [14–16] as well as those of dynamic phenomena such as spin waves [17–21]. Recent experiments demonstrated that NV magnetometry has the sensitivity required for imaging the static magnetization of monolayer van der Waals magnets [22]. Here, we develop

NV-based magnetic resonance imaging into a platform for studying coherent spin waves via the gigahertz magnetic fields that they generate.

4.2. RESULTS

Our imaging platform consists of a diamond chip hosting a dense layer of shallowly implanted NV spins. We position this chip onto a thin film of yttrium iron garnet (YIG) — a ferrimagnetic insulator with record-high magnetic quality (Fig. 4.1A-B) [23]. The typical distance between the diamond and the magnetic film is ~ 1 µm (Supplementary Material). We excite spin waves using microwave striplines microfabricated onto the YIG. When the spin-wave frequency matches an NV electron spin resonance (ESR) frequency, the oscillating magnetic stray field B_{SW} drives NV spin transitions [17, 19] that we detect through the NV's spin-dependent photoluminescence (Materials and Methods). By tuning the external static magnetic field B_0, we sweep the NV ESR frequencies through the spin-wave band, thereby probing spin waves with different wavelength (Fig. 4.1C).

We start by characterizing the NV photoluminescence as a function of B_0 and the frequency ω_{MW} of a microwave drive current sent through the stripline, at a distance of ~ 5 µm from the stripline edge (Fig. 4.1D). This microwave current not only generates an oscillating magnetic field that drives ESR transitions of the NV spins directly but also excites spin waves in the YIG film that can drive NV ESR transitions via their magnetic stray field (Fig. 4.1A). The dips in the observed NV photoluminescence correspond to the ESR frequencies of the NV spins in the diamond (Fig. 4.1D; Materials and Methods). We observe an enhanced contrast for the ω_- transition when $B < B_0^{(2)}$. In this region, the excited spin waves efficiently drive the ω_- ESR transition.

We image the spin waves excited by the stripline in the YIG film by characterizing the contrast of the ω_- ESR transition as a function of the distance to the stripline (Fig. 4.2A). We do so by tuning the magnetic field such that the ω_- frequency is 2.17 GHz, i.e., 160 MHz above the bottom of the spin-wave band, thereby exciting spin waves in the film. To gain the phase sensitivity required for detecting the individual wavefronts of these propagating spin waves, we let their stray field interfere with an additional, externally applied microwave magnetic field B_{REF} that is spatially homogeneous and has the same frequency (Materials and Methods). As formulated mathematically below, this interference leads to a spatial standing-wave pattern in the total magnetic field that drives the NV ESR transition with a spatial periodicity equal to the spin-wave wavelength. We can thus rapidly visualize the spin waves by measuring the ratio between the NV photoluminescence with and without applied microwaves (Fig. 4.2A).

Quantifying the amplitude of a spin wave is a challenging task for any technique because the coupling between spin wave and probe is often not well known. With NV magnetometry, however, we accurately measure the microwave magnetic field generated by a spin wave as described by Maxwell's equations. We can therefore determine the amplitude of a spin wave of known direction and ellipticity with high confidence by solving a well-defined inverse problem.

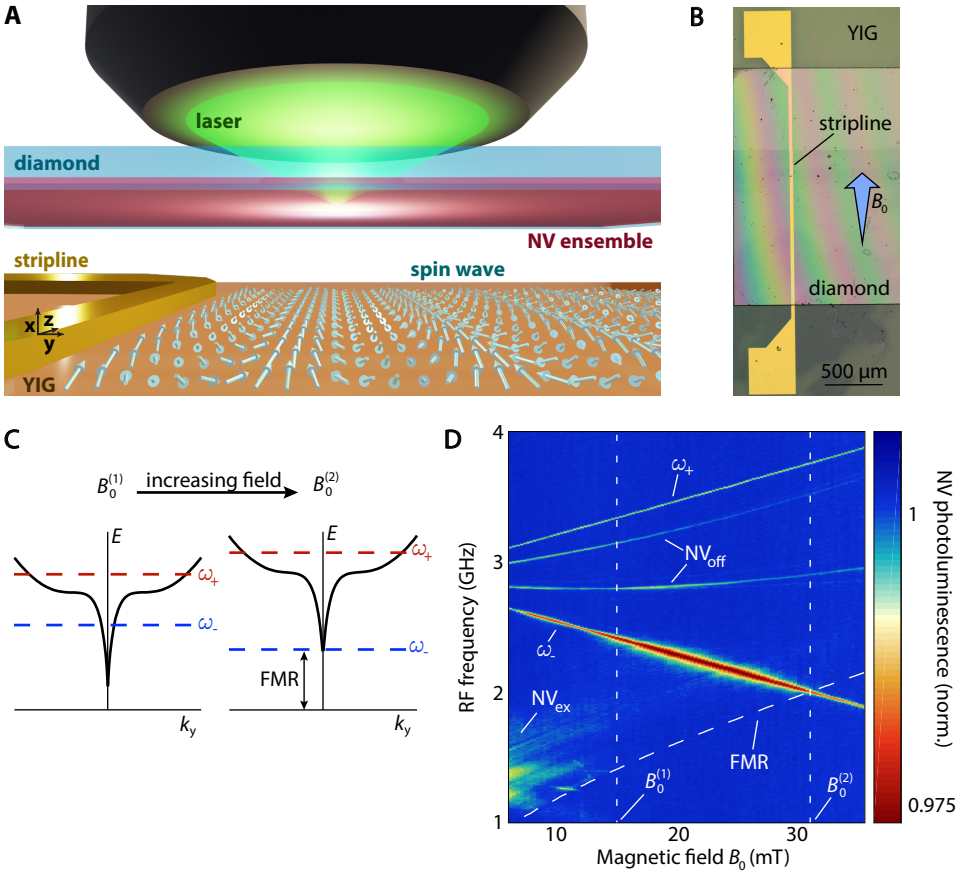

Figure 4.1: Imaging spin waves using NV spins in diamond. (**A**) A diamond hosting a layer of NV spins implanted at 20 nm below its surface is placed onto a film of YIG (thickness of 245 nm) grown on gadolinium gallium garnet (GGG). The NVs detect the magnetic fields of stripline-excited spin waves. (**B**) NV-containing diamond (thickness of ~ 40 µm) on YIG with gold stripline. B_0 is applied along the stripline at $\phi = 35°$ relative to the sample plane, aligning it with one of the four possible NV orientations. (**C**) The NV ESR frequencies $\omega_\pm$ are swept over the Damon-Eshbach spin-wave dispersion (black line) by tuning B_0. For any $B_0^{(1)} < B_0^{(2)}$, ω_- is resonant with spin waves of finite wavelength. At $B_0 < B_0^{(2)}$, ω_- is resonant with the ferromagnetic resonance (FMR). (**D**) Normalized NV photoluminescence versus B_0 and microwave drive frequency, measured at ~ 5 µm from a 2.5 µm-wide stripline. Indicated are the electronic ground-state ESR transitions $\omega_\pm$ (NV_{off}) of the NVs aligned (not aligned) with B_0. An electronic excited-state ESR transition (NV_{ex}) is visible because of the continuous optical and microwave excitation and identified through its location at $\omega_+/2$ [12]. The FMR is calculated from the independently determined saturation magnetization (Supplementary Material).

To illustrate the concept, we formulate the magnetic stray field of a spin wave traveling perpendicularly to the static magnetization (such as the one in Fig. 4.2B) in the reference frame depicted in Fig. 4.1A with transverse magnetization

$$\mathbf{m}_\perp(y) = m_\perp^0 \mathrm{Re}\left\{e^{i(k_y y-\omega t)}(\hat{\mathbf{y}} - i\eta\hat{\mathbf{x}})\right\} \tag{4.1}$$

where k_y, ω, and η are the wave number, angular frequency, and ellipticity of the spin wave, respectively; t is the time; and hats denote unit vectors. This spin wave produces a magnetic stray field above the film that rotates in the xy plane (see the Supplementary Material and [24]).

$$\mathbf{B}_{SW}(y) = -B_{SW}^0 \mathrm{Re}\left\{e^{i(k_y y-\omega t)}(\hat{\mathbf{y}} + i\,\mathrm{sgn}(k_y)\hat{\mathbf{x}})\right\} \tag{4.2}$$

where $B_{SW}^0 = \mu_0 m_\perp^0 \left[1+\mathrm{sgn}(k_y)\eta\right]|\mathbf{k}|d e^{-|k_y|x_0}/2$, x_0 is the NV-YIG distance, and d is the thickness of the YIG film.

The handedness of $\mathbf{B}_{SW}$ is opposite to that of $\mathbf{m}_\perp$ for a spin wave traveling to the right (i.e., with $k_y > 0$; as in Fig. 4.2B), which drives the ω_- (rather than the ω_+) NV spin transition (Supplementary Material). Moreover, the amplitude B_{SW}^0 depends on the propagation direction and degree of ellipticity η of the spin wave: Those traveling to the right (left) generate a stronger field above (below) the magnetic film. Therefore, only the ω_- transition of NV centers to the right of the stripline in Fig. 4.2B is excited (Supplementary Material). The resulting NV spin rotation rate (Rabi frequency) ω_{Rabi} is determined by the interference between the spin-wave field and the reference field B_{REF}

$$\omega_{Rabi} = \sqrt{2}\gamma|B_{SW}^0 \cos^2\left(\frac{\phi}{2}\right)e^{ik_y y} - B_{REF}| \tag{4.3}$$

where $\phi = 35°$ is the angle with respect to (w.r.t.) the film of the NV centers used in Fig. 4.2 and $\gamma/2\pi = 28$ GHz/T is the (modulus of the) electron gyromagnetic ratio. Fitting the data in Fig. 4.2B by Eq. 4.3(including a spatial decay; see the Supplementary Material), we extract a spin-wave amplitude $m_\perp^0 = 0.033(1)\ M_s$ at the location of the stripline and a decay length of 1.2(1) mm, corresponding to a Gilbert damping parameter $1.2(1)\cdot 10^{-4}$, which is similar to the typically reported $1\cdot 10^{-4}$ for films of similar thickness [25].

By tuning the externally applied magnetic field, we sweep the NV ESR frequency through the spin-wave band and access spin waves with different wavelengths (Fig. 4.3A), as schematically described in Fig. 4.1C. In Fig. 4.3A-B, we visualize the individual spin-wave fronts using the interference between the direct stripline field and the stray field of the propagating spin wave. We extract the spin-wave dispersion from the frequency dependence of the wavelength (Fig. 4.3C). This dispersion matches the one calculated using values of the saturation magnetization M_s and film thickness d determined by independent measurements (Supplementary Material).

Travelling spin-wave packets can be used for pulsed quantum control of distant spins such as those of the NV centers [19, 20]. Understanding the distance-dependent response of the spins to an applied control sequence requires knowledge of the spin-wave

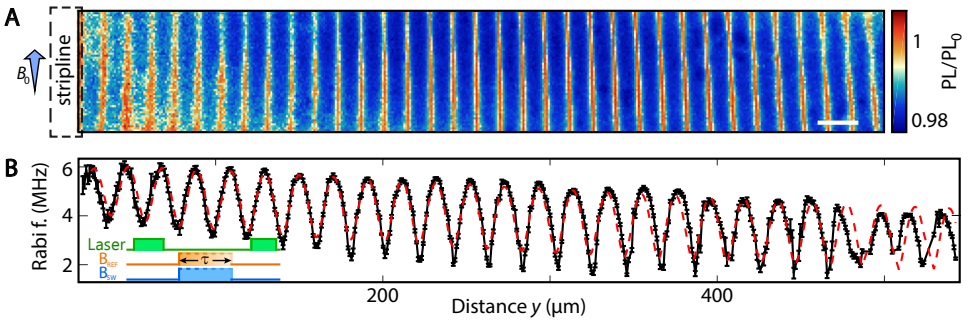

Figure 4.2: Imaging coherent spin waves. (**A**) Spatial ESR contrast at $B_0 = 25$ mT when a spin wave of frequency $\omega_{SW} = \omega_- = 2\pi \times 2.17$ GHz is excited by a microwave current in the stripline (length of 2 mm, width of 30 μm, and thickness of 200 nm) at the left image edge. The NV photoluminescence with applied microwaves (PL) is normalized to that without applied microwaves (PL$_0$). The NV-YIG distance at the stripline was 1.8(2) μm, determined by measuring the field of a DC stripline current (Supplementary Material). Scale bar, 20 μm. (**B**) Rabi frequency $\omega_{Rabi}/2\pi$ versus distance from the stripline. $\omega_{SW} = \omega_- = 2\pi \times 2.11$ GHz, $B_0 = 27$ mT. In (A) and (B), the microwaves were split between the stripline and a bonding wire, located ≈100 μm above the YIG and oriented along y to generate a spatially homogeneous field B_{REF}, creating an interference pattern (see text). Red line: Fit to a model including the field of the stripline, the bonding wire, and the spin waves (section 4.5.3.3). Inset: Measurement sequence. Laser pulses (1 μs) are used to initialize and read out the NV spins. Microwave pulses (duration τ) drive Rabi oscillations. ω_{Rabi} was calculated from the measured $\omega_{Rabi,0}$ using $\omega_{Rabi} = \sqrt{\omega_{Rabi,0}^2 - \Delta^2}$ to account for a $\Delta = 2\pi \times 1.5$ MHz detuning between the drive frequency and the two hyperfine-split ESR resonances caused by the ^{15}N nuclear spin.

group velocity. We demonstrate a time-domain characterization of the spin-wave propagation using pulsed control of the NV spins (Fig. 4.3D-E). In our measurement scheme (Fig. 4.3D), the NV spins at a target distance from the stripline are prepared in $m_s = 0$ using a green laser pulse. A spin-wave pulse (excited by the stripline) flips the NV spins into the dark $m_s = -1$ state only if it arrives either before or after a set of two reference pulses acting on the $0 \leftrightarrow +1$ transition (generated by a wire above the sample), resulting in low photoluminescence upon spin readout. In contrast, if the spin-wave pulse reaches the NVs between the two reference pulses, then it does not affect the NV spins because they are in $m_s = +1$ due to the first reference pulse. The second reference pulse subsequently flips the spin back to the bright $m_s = 0$ state, resulting in high photoluminescence upon spin readout. Measurements as a function of time between spin-wave and reference pulses and distance from the stripline reveal the spin-wave packet in the time domain and allow the extraction of the group velocity (Fig. 4.3E). We find a velocity of 3.6(2) km/s at a frequency of 2.169 GHz and a wavelength of 12 μm, consistent with the YIG spin-wave dispersion.

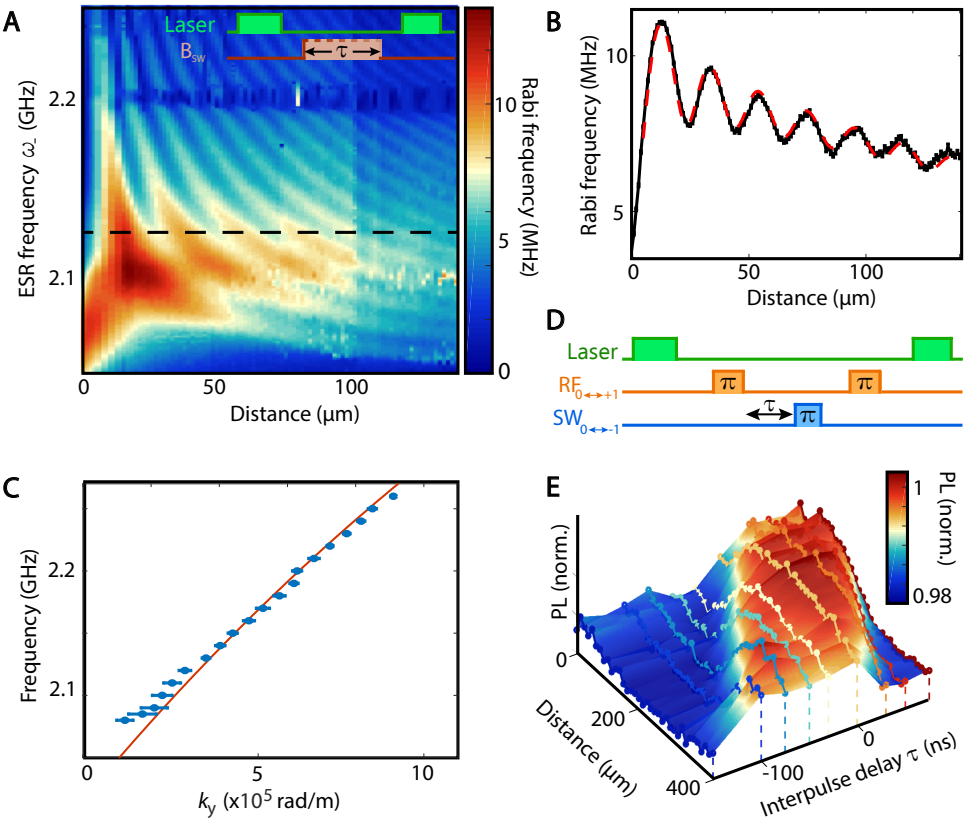

Figure 4.3: Spin-wave dispersion in the space and time domains. (**A**) NV Rabi frequency versus microwave drive frequency and distance from the stripline. The feature at 2.2 GHz matches the first perpendicular spin-wave mode (Supplementary Material). Inset: Measurement sequence. (**B**) Linecut of (A) with fit (red line) at 2.119 GHz. (**C**) Blue dots: Spin-wave frequency versus wave number extracted from (A). Red line: Calculated spin-wave dispersion. (**D**) Pulse sequence for studying spin-wave packets in the time domain [see text for details; data in (E)]: Laser pulses (1 μs) are used for NV spin initialization and readout. Two reference (RF) π pulses separated by 100 ns are applied at the $0 \leftrightarrow +1$ ESR frequency via a wire above the sample. After a time τ from the end of the first RF pulse, a spin wave–mediated π-pulse (SW) is generated at the $0 \leftrightarrow -1$ ESR frequency. (**E**) Normalized NV photoluminescence (PL) during the first 400 ns of the laser readout pulse [see (D)] versus distance from the stripline and delay time π. Negative τ indicates a spin-wave packet generated before the first RF pulse. For example, for $\tau = -100$ ns (i.e., the spin-wave pulse is generated 100 ns before the first RF pulse), the signal rises at 360 μm, indicating a spin-wave group velocity of 3.6 km/s. Circles, data; colored surface, interpolation.

The 2-mm-long stripline used in Figs. 4.2 and 4.3 corresponds to an effectively one-dimensional situation. We now turn to spin waves injected by a shorter stripline with a length comparable to the scanned area (Fig. 4.4A). We observe a focused emission pattern that is dominated by spin-wave beams traveling at specific angles (Fig. 4.4B-C). Such "caustics" occur when the dispersion is strongly anisotropic [26, 27]. They can be understood in terms of stationary points in the isofrequency curves in reciprocal space (Fig. 4.4D). In optics, such an isofrequency curve $k_z = k_z(k_y)$ is called "slowness" curve, because it is perpendicular to the group velocity $\mathbf{v}_G = \nabla_{\mathbf{k}}\omega(\mathbf{k})$. The states for which the angle of the group velocity $\theta = -\arctan(dk_z(k_y)/dk_y)$ is stationary along the curve, i.e., when $d\theta/dk_y \propto d^2k_z(k_y)/dk_y^2 = 0$, dominate emission, generating high-intensity spin-wave beams. The external magnetic field and the drive frequency can tune the beam direction and intensity [26, 27], providing opportunities to optimize the efficiency of spin wave–mediated magnetic field driving of distant spins at target locations.

Last, we image the interference between spin waves excited by two adjacent striplines on the YIG chip (Fig. 4.4, E and F), which shows rich interference patterns radiating from the three crossing points of the main caustics (i.e., ~ 80 μm from the striplines edge). The strongly anisotropic spin-wave dispersion causes a triangular "dark" region between the striplines in which no spin waves are detected, because spin waves traveling at small angles with respect to the equilibrium magnetization direction or having large wave numbers are neither efficiently excited (when the wavelength is shorter than the half-width of the stripline) nor efficiently detected due to the ~ 1 μm NV-sample distance. The downward directionality of the observed spin-wave patterns has two causes: The chiral spin-wave field has the correct handedness to drive the ω_- NV transition, and the handedness of the stripline field excites downward-propagating spin waves more efficiently (Supplementary Material). We note that these waves are not intrinsically directional because their wavelength far exceeds the film thickness [28], in contrast with Damon-Eshbach surface waves in thick films [29]. The observed directionality and interference patterns agree well with linear response calculations of the nonlocal dynamic susceptibility and the spatial profile of the microwave drive field, as described in the Supplementary Material. These quantitative measurements of the spin wave–generated rotating magnetic stray fields illustrate the power of NV-based magnetic resonance imaging in magnonics.

4.3. DISCUSSION

Our results demonstrate that ensembles of NV spins in diamonds enable quantitative, phase-sensitive magnetic imaging of coherent spin waves in thin-film magnets. A theoretical analysis explains the NV sensor signals in terms of the rotating stray fields generated by spin waves that are excited unidirectionally by the stripline magnetic field. In contrast to other spin-wave imaging techniques, our technique images spin waves by their microwave magnetic stray fields. This does not require a specific spin-photon or spin-electron interaction and enables imaging spin waves through optically opaque materials. These capabilities provide new opportunities, e.g., for studying top-gated materials and the interaction of spin waves with magnetic and nonmagnetic materials placed

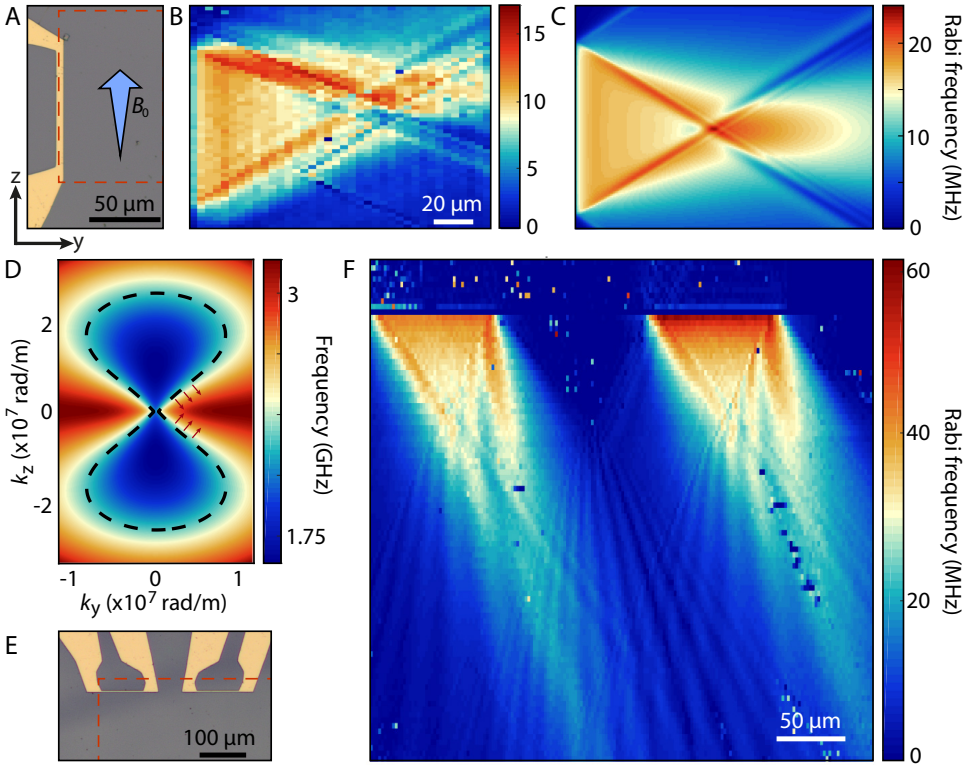

Figure 4.4: Imaging interference and caustics of spin waves excited by one and two short striplines. (**A**) Optical micrograph of the stripline (width of 5 µm) used to excite spin waves. The dashed red lines indicate the region where (B) is acquired. (**B**) Rabi frequency map corresponding to the dashed region of (A) for $B_0 = 27.1$ mT and $\omega/2\pi = 2.11$ GHz. The small asymmetry is attributed to a small misalignment of B_0 with respect to the striplines. (**C**) Simulation of the emission pattern observed in (B). (**D**) Calculated two-dimensional spin-wave dispersion relation $\omega(k_y, k_z)/2\pi$ at $B_0 = 20.5$ mT. The dashed line is an isofrequency contour at 2.292 GHz, indicating which wave vectors can be excited at this frequency and field. Red arrows indicate the direction of the spin-wave caustics. (**E**) Optical micrographs of the two injector striplines of width 2.5 µm. The dashed lines indicates the region where (F) is acquired. (**F**) Rabi frequency map under simultaneous driving of the two striplines, showing unidirectional excitation of autofocused spin-wave patterns that interfere and drive NV Rabi oscillations via their chiral magnetic stray fields.

on top of a magnetic film, which play an important role for spin-wave excitation and damping and form the basis for nonreciprocal devices [30]. NV magnetometry also allows high-resolution imaging of electric currents [31], enabling spatial studies of the interaction between spin waves and charge transport.

Both the NV-sample distance and the optical resolution of our microscope limit the resolution of our technique. The typical NV-magnet distances are here 0.5 to 2 μm (limited by, e.g., dust particles), comparable to our diffraction-limited optical resolution. Shallow NV centers in diamond chips that are wafer-bonded to (i.e., in direct contact with) a magnetic sample should allow the detection of spin waves with wavelengths comparable to the implantation depth of the NV centers of a few nanometers [32]—albeit without phase sensitivity. This requires resonance between the spin waves and the NV sensors, e.g., by tuning a magnetic field and/or magnetic anisotropies. This may be difficult for magnetically hard materials. We can probe nonresonant spin waves by detecting the Stark shift that they impart on the sensor spins [33] or by detecting intraband spin-wave transitions using NV spin relaxometry [34]. Phase-sensitive imaging of spin waves with wavelengths below the diffraction limit could be enabled using specialized NV control sequences such as phase encoding schemes [35]. Furthermore, the techniques presented here are directly transferrable to single-NV scanning probe microscopes with real-space resolution on the 10-nm scale [36].

Our results pave the way for studying spin waves in other magnetic material systems such as magnetic nanodevices and atomically thin magnets. NV magnetometry works at cryogenic temperatures [37–39], allowing studies of magnets with low Curie temperatures such as complex oxide or van der Waals magnets. Because the dipole density per unit area $M_s d = 3.6 \cdot 10^3$ μ_B/nm^2 of the YIG film studied here is only about two orders of magnitude above the 16 μ_B/nm^2 of the monolayer van der Waals magnet CrI_3 [22], the magnetic stray fields generated by spin waves in such monolayer magnets are within the sensitivity range of NV-based magnetic imaging. The sensitivity of our technique is rooted in measuring the sum of a reference field and the spin-wave field. A good strategy for measuring weak spinwave fields is to apply a strong reference field and measure the variations in the Rabi frequency caused by the spin-wave field, because Rabi frequency variations of ~ 100 kHz can easily be detected (the average error bar in Fig. 2B is 75 kHz). We can further increase the sensitivity by applying a stronger reference field, which decouples the NV spin from noise sources [40]. Increasing the microwave drive current and reducing the NV-sample distance (for instance, by depositing a van der Waals material directly onto the diamond [41]) would further increase the detection capability.

ACKNOWLEDGEMENTS

Funding: This work was supported by the Dutch Research Council (NWO) as part of the Frontiers of Nanoscience (NanoFront) program through NWO Projectruimte grant 680.91.115, JSPS KAKENHI grant no. 19H006450, and Kavli Institute of Nanoscience Delft.

Author contributions: I.B., J.J.C., and T.v.d.S. designed the experiment. I.B. fabricated the diamond-YIG samples, realized the imaging setup, performed the NV measurements,

and analyzed the data. B.G.S. prepared the diamonds. C.C.P. performed the vector network analyzer (VNA) measurements, for which J.J.C. fabricated the samples. T.Y., Y.M.B., and G.E.W.B. developed the theoretical model describing spin-wave caustics and interference. I.B. and T.v.d.S. wrote the manuscript with help from all coauthors. J.A. contributed to the discussions of the results and the manuscript.
Competing interests: The authors declare that they have no competing interests.
Data and materials availability: All data contained in the figures are available at Zenodo.org with the identifier 10.5281/zenodo.4005488. Additional data related to this paper may be requested from the authors.

4.4. MATERIALS AND METHODS

4.4.1. SAMPLE FABRICATION

The diamond samples used in this work are chemical vapor deposition (CVD)–grown, electronic-grade type IIa diamonds (Element 6), laser-cut, and polished down to 2 mm × 2 mm × 0.05 mm chips (Almax easyLab). These chips were cleaned with nitric acid, and the top ~ 5 μm were removed using inductively-coupled plasma (ICP) reactive ion etching (30 min Ar/Cl, 20 min O_2) to mitigate polishing damage. The chips were subsequently implanted with ^{15}N ions at 6 keV with a dose of 1 $\times 10^{13}$ ions/cm^2 (INNOViON), tri-acid cleaned (mixture of nitric, sulfuric, and perchloric acid, 1:1:1), annealed at 800°C for 4 hours at 10^{-6} mbar, and tri-acid cleaned again to remove possibly graphitized layers on the surface, resulting in an estimated density of NV centers of ~ 1×10^{11} NV/cm^2 at a depth of ~10 to 20 nm.

The YIG films were 245 nm thick, grown on gadolinium gallium garnet (GGG) substrates by liquid-phase epitaxy (Matesy GmbH). Before stripline fabrication, the YIG/GGG chips were sonicated in acetone and cleaned for a few seconds in an O_2 descum plasma to remove contaminants. Striplines for spin-wave excitation were fabricated directly onto the YIG films by e-beam lithography using a PMMA(A8 495)/PMMA(A3 950) double-layer resist and subsequent e-beam evaporation of Cr/Au (5 nm/200 nm). To attach an NV-containing diamond to the YIG film, a small droplet of isopropanol was deposited onto the YIG, on top of which a diamond chip was placed, with the NV surface facing down. The diamond chip was gently pressed down until the isopropyl alcohol had evaporated [42]. The resulting NV-YIG distance was measured to be 1.8(2) μm (see fig. 4.5).

4.4.2. MEASUREMENT SETUP

The optical setup used for all the measurements was a homebuilt confocal microscope. A 515-nm laser (Cobolt 06-MLD) was used for optical excitation of the NV centers, focused to a diffraction-limited spot by an Olympus 50×, numerical aperture = 0.95 objective. The NV luminescence was collected by the same objective, separated from the excitation light by a Semrock dichroic mirror and long-pass filter (617 nm cutoff), spatially filtered by a pinhole, and detected using a single-photon counting module (Laser Components). The microwaves signals used for driving NVs and spin waves were generated using Rohde & Schwarz microwave generators (SGS100A). The reference field B_{REF} used to produce the interference pattern in Fig. 4.2 was generated by a wire located ~ 200 μm

above the diamond and oriented perpendicularly to the stripline. To simultaneously drive the pair of striplines in Fig. 4, the microwave excitation was split using a Mini-Circuits power combiner (ZFRSC-123-S+). A National Instruments data acquisition card was used for triggering the data acquisition, while a SpinCore programmable pulse generator (PulseBlaster ESR-PRO 500) was used to control the timing sequences of the laser excitation, microwaves, and detection window. The photons were collected during the first 300 to 400 ns of the laser readout pulse, which was kept fixed to 1 µs. All measurements were performed at room temperature.

4.4.3. NV MAGNETOMETRY

The NV spins are initialized and read out using nonresonant optical excitation at 515 nm. To measure NV spin rotations (Rabi oscillations), we first apply a ~ 1 µs green laser pulse to polarize the NV spin into the $m_s = 0$ state. A subsequently applied microwave magnetic field resonant with an NV ESR frequency drives Rabi oscillations between the corresponding NV spin states ($m_s = 0$ and -1 in Fig. 4.2B). The NV spin state is read out by applying a laser pulse and measuring the spin-dependent photoluminescence that results from spin-selective nonradiative decay via a metastable singlet state. The ESR frequencies of the four NV families (Fig. 4.1D) in a magnetic field B_0 are determined by the NV spin Hamiltonian $H = DS_z^2 + \gamma \mathbf{B}_0 \cdot \mathbf{S}$, where γ is the electron gyromagnetic ratio, D is the zero-field splitting (2.87 GHz), and $S_{(i=x,y,z)}$ is the Pauli spin matrices for a spin 1. We apply the magnetic field B_0 using a small permanent magnet (diameter, 1 cm; height, 2 cm).

4.4.4. WAVELENGTH OF THE SPIN WAVES DRIVING NV RABI OSCILLATIONS

We excite spin waves at a frequency that matches the ω_- ESR transition of the NV spins, allowing us to detect the spin waves via the resulting NV Rabi oscillations. Hence, for a given field B_0 applied along the NV axis, the wave number of the spin waves driving Rabi oscillations is determined by equating the NV frequency $\omega_-/2\pi = D - \gamma B_0$ to the spin-wave frequency given by the spin-wave dispersion (eq. 4.14)

$$\frac{\omega(B_0,k)}{\gamma\mu_0 M_s} = \sqrt{\left(\frac{B_0\cos\theta}{\mu_0 M_s} + \alpha_{ex}k^2 + \frac{1-e^{-|k_y|d}}{|k_y|d}\right)\left(\frac{B_0\cos\theta}{\mu_0 M_s} + \alpha_{ex}k^2 + \frac{k_y^2}{k^2}\left(1 - \frac{1-e^{-|k_y|d}}{|k_y|d}\right)\right)} \tag{4.4}$$

where k is the SW wave number; k_y is its in-plane component perpendicular to the static magnetization; μ_0 is the magnetic permeability of vacuum; and M_s, $\alpha_{ex} = 3.0 \cdot 10^{-16}$ m^2, and d are the YIG saturation magnetization, exchange constant [23], and thickness, respectively.

4.5. SUPPLEMENTARY MATERIAL

4.5.1. DETERMINATION OF THE NV-YIG DISTANCE

The distance x_0 between the YIG surface and the NV sensing layer is an important parameter for the reconstruction of spin-wave amplitude from the detected field (Fig. 4.2) of the main text). We determined x_0 by sending a DC current I_{DC} through the stripline and characterizing the resulting magnetic field $\mathbf{B}_{DC}(x_0, y)$ using the NV sensing layer.

This field causes spatially dependent shifts in the NV ESR frequencies (Fig. 4.5A-B) from which we can extract x_0 as described next. Considering an infinitely thin stripline of width w with its center at $x = y = 0$, the stripline field is given by

$$\mathbf{B}_{DC}(x_0, y) = \frac{\mu_0 I_{DC}}{2\pi w}\left(\frac{1}{2}\ln\left(\frac{x_0^2 + (y + w/2)^2}{x_0^2 + (y - w/2)^2}\right)\hat{\mathbf{x}} + \arctan\left(\frac{w x_0}{x_0^2 + y^2 - (w/2)^2}\right)\hat{\mathbf{y}}\right) \tag{4.5}$$

To facilitate the analysis of the ESR spectra, we also applied a small bias field $\mathbf{B}_0$ to increase the splitting of the 8 ESR transitions of the 4 NV families. From the total field $\mathbf{B} = \mathbf{B}_0 + \mathbf{B}_{DC}$, we calculate the ESR frequencies for the 4 NV families by diagonalizing the NV spin Hamiltonian $H = DS_z^2 + \gamma(B_\parallel S_z + B_\perp S_x)$, where $B_\parallel$ is the projection of $\mathbf{B}$ onto the NV axis and $B_\perp = \sqrt{B^2 - B_\parallel^2}$. From the fit to this model (Fig. 4.5C), we extract $\mathbf{B_0}$ = (0.461(3), 3.568(3), 0.626(3)) mT, D = 2.872(1) GHz and x_0 = 1.8(2) µm. For the sample in Fig. 4 we used an alternative, optical method to determine the distance, focusing the excitation laser first on the YIG surface and then on the NV layer, reading off the change in the position of the microscope objective from its closed-loop piezo-controller, measuring $x_{0,\text{Sample2}}$ = 1.0(3) µm.

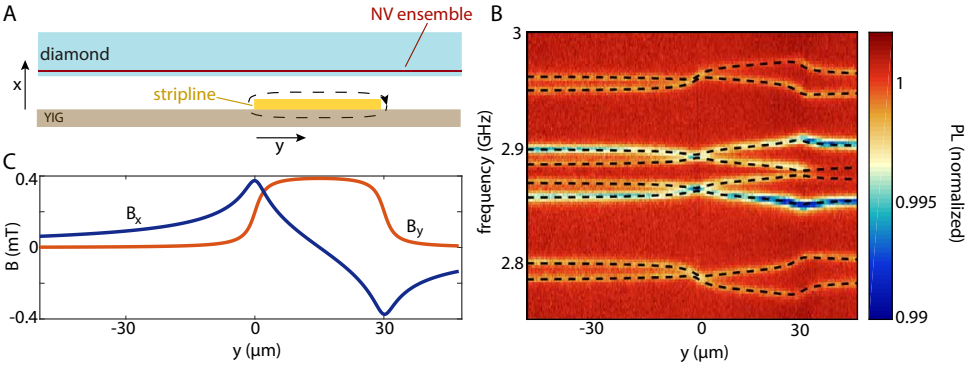

Figure 4.5: Determination of the YIG-NV distance. (**A**) Idea of the measurement. The diamond is located at a height x above the current-carrying stripline fabricated on the YIG. ESR spectra are measured along a line perpendicular to the stripline. The current in the stripline generates a magnetic field (dashed black line), causing a shift of the NV ESR frequencies. (**B**) NV ESR spectra measured along a line oriented perpendicularly to the stripline (which is located between $y = 0$ and $y = 30$ µm). The eight dips in the photoluminescence (PL) are caused by the ESR transitions of the four NV families having different orientations in the diamond crystal lattice. (**C**) Stripline magnetic field in the NV layer corresponding to the values extracted from the fit.

4.5.2. DETERMINATION OF M_s AND THICKNESS OF YIG WITH VNA MEASUREMENTS

The YIG saturation magnetization M_s and thickness d are important parameters for analyzing the spin-wave dispersion. Here we describe the extraction of these parameters

using vector network analyzer (VNA) measurements.

We flip-chip a YIG chip on the central conductor of a coplanar waveguide (CPW) and use a VNA to measure the microwave transmission S_{21} through the CPW as a function of a magnetic field B_0 applied in-plane and parallel to the central conductor of the CPW (Fig. 4.6 A). When the frequency matches the YIG FMR, energy is absorbed and S_{21} decreases. We extract $M_s = 1.42(1) \cdot 10^5$ A/m by fitting the data with the Kittel equation $\omega = \gamma\sqrt{B_0(B_0 + \mu_0 M_s)}$.

We determine the thickness of the YIG chip from the frequency of the first perpendicular standing spin-wave mode (PSSW) [43].To extract the frequency of the first PSSW, we measure the spin-wave mediated transmission of microwaves between two striplines using the VNA (Fig. 4.6 B-C). The PSSW manifests as a small dip in the transmission (indicated by the dashed black line in Fig. 4.6 B and the black arrow in Fig. 4.6 D). To extract the thickness d, we calculate the PSSW frequency at each field for fixed M_s and different values of the thickness using [44]. The best match is reached for $d = 245(5)$ nm.

4.5.3. EFFECT OF THE SPIN WAVE STRAY FIELD ON THE NV SPINS

In this section we derive the NV Rabi frequency due to the stray fields from spin waves excited in the YIG by a stripline carrying an oscillating current. In section 4.5.3.2 we present the magnetization profile excited by the stripline magnetic field, based on the spin susceptibility of the YIG. In section 4.5.3.3 we provide the dipolar field generated by the magnetization oscillations at the NV centers and determine their Rabi frequency by evaluating the efficiency of the field in driving the NV spins, including the chirality of the spin-wave field. In section 4.5.3.6, we extend the results obtained to the case of two adjacent striplines and calculate the interference pattern. Our theoretical framework captures and explains several effects visible in the data, such as the spin wave focussing and caustics beams, as well as the interference fringes.

MODEL AND PARAMETERS

We use the reference frame depicted in Fig. 4.1 of the main text. Additionally, the length, width and thickness of the stripline are referred to as l, w and δ, respectively, the thickness of the yttrium iron garnet (YIG) film is d, and the NV-YIG distance is x_0. The static magnetic field B_0 is always applied at a ϕ=35° angle with respect to the sample plane and parallel to the striplines. Because B_0 in the experiments of Figs. 4.2-4.4 does not exceed 27 mT, which is much smaller than the YIG saturation magnetization $\mu_0 M_s \approx 178$ mT, the static magnetization of the film only tilts out of plane by a small angle $B_0 \sin\phi/(\mu_0 M_s) \lessapprox 5°$. We therefore disregard the out-of-plane component of the static magnetizaton and magnetic field B_0 in the calculations. We use the parameters $w = 2.5$ µm, $\delta = 200$ nm, $l = 88$ µm, $d = 245$ nm and $x_0 = 1$ µm. The striplines in Fig. 4.4E-F of the main text are 110 µm apart and driven with a phase difference of π.

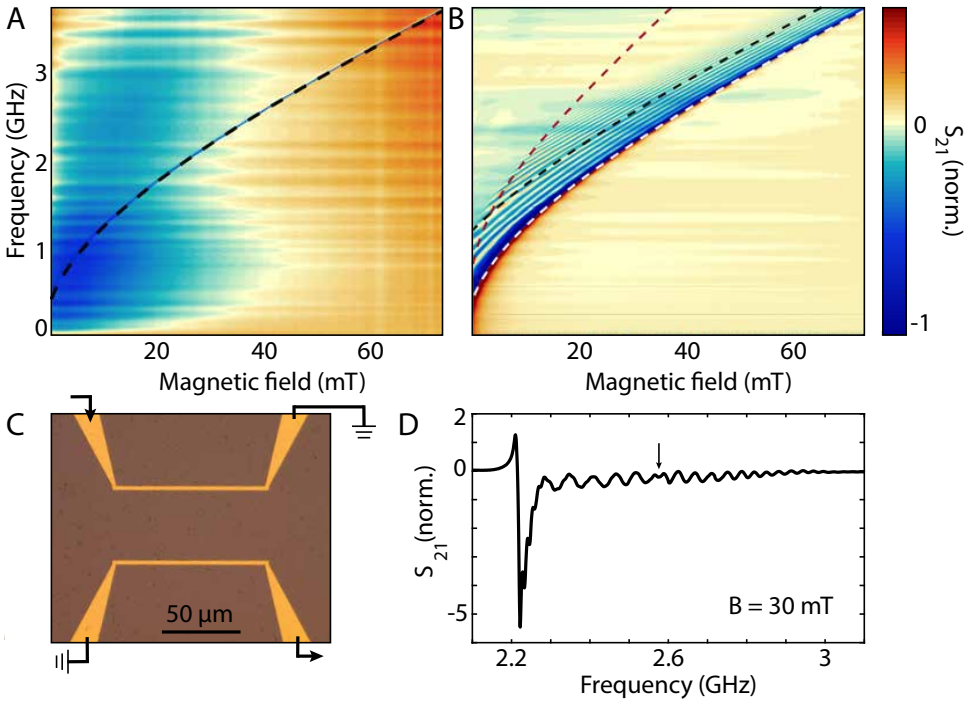

Figure 4.6: VNA-FMR detection of spin waves to determine M_s and thickness of the YIG chip. (**A**) Transmission $S_{21}(B,\omega)$ through the central conductor of a CPW on top of which a YIG chip is placed. The absorption of YIG at the FMR (dark blue line in the data) is extremely sharp (FWHM<10 MHz). The dashed black line is calculated using the extracted value of $M_s = 1.42 \cdot 10^5$ A/m. (**B**) $S_{21}(B,\omega)$ mediated by spin waves across the device shown in (C). The white and black dashed lines are the calculated frequencies of the FMR and 1st-order PSSW, respectively. The red dashed line indicates a frequency that is twice that of the calculated band minimum. Above this frequency, three-magnon scattering becomes allowed, which may contribute to the observed vanishing of the spin-wave mediated transmission above this frequency. (**C**) Device used to obtain the measurement in (B). The two gold striplines fabricated on YIG and connected to the input and output of the VNA as indicated by the arrows. Stripline width = 2.5 µm, thickness = 200 nm. (**D**) Vertical linecut of (B) at 30 mT, showing the FMR absorption dip followed by several oscillations and the PSSW, indicated by the black arrow.

MAGNETIZATION EXCITED BY A MICROWAVE STRIPLINE OF FINITE LENGTH

Stripline magnetic field

Two striplines $i = \{1,2\}$ carrying a current density $\mathbf{J}_i(\mathbf{r},\omega)$ with frequency ω generate the vector potentials [45]

$$\mathbf{A}_i(\mathbf{r},\omega) = \frac{\mu_0}{4\pi}\int d\mathbf{r}'\mathbf{J}_i(\mathbf{r}',\omega)\frac{e^{ik|\mathbf{r}-\mathbf{r}'|}}{|\mathbf{r}-\mathbf{r}'|}, \tag{4.6}$$

parallel to the direction of the current (the z-direction). μ_0 is the vacuum permeability and $k = \omega/c$. Substituting the Weyl identity [46],

$$\frac{e^{ik\sqrt{(x-x')^2+(y-y')^2+(z-z')^2}}}{\sqrt{(x-x')^2+(y-y')^2+(z-z')^2}} = \frac{i}{2\pi}\int dk_y dk_z \frac{e^{ik_x|x-x'|+ik_y(y-y')+ik_z(z-z')}}{k_x}, \tag{4.7}$$

where $k = \sqrt{k_x^2+k_y^2+k_z^2}$ (and hence $k_x = \sqrt{k^2-k_y^2-k_z^2}$), the Fourier components of the magnetic field $\mu_0(H_x,H_y)^{(i)} = (\partial A_z/\partial y, -\partial A_z/\partial x)^{(i)}$ in reciprocal space are

$$H_x^{(i)}(x;k_y,k_z) = 2iJ_i(\omega)\frac{e^{-ik_x x}}{k_x}\frac{e^{ik_x\delta}-1}{k_x}\sin\left(k_y\frac{w}{2}\right)\frac{\sin(k_z l_i/2)}{k_z}e^{-ik_z z_i}, \tag{4.8}$$

$$H_y^{(i)}(x;k_y,k_z) = 2iJ_i(\omega)\frac{e^{-ik_x x}}{k_x}\frac{e^{ik_x\delta}-1}{k_y}\sin\left(k_y\frac{w}{2}\right)\frac{\sin(k_z l_i/2)}{k_z}e^{-ik_z z_i}, \tag{4.9}$$

where $k_x = \sqrt{(\omega/c)^2-k_y^2-k_z^2}$, z_i are the z-coordinates of the centers of the striplines and the total current is given by $J_i w\delta$. The generated magnetic field is perpendicular to the stripline axis, i.e. $H_z = 0$, and $k_x H_x(x;k_y,k_z) = k_y H_y(x;k_y,k_z)$. Since $l \gg w$, the magnetic field oscillates as function of k_z with a short period of $4\pi/l$, while it oscillates with k_y with a much longer period of $4\pi/w$ (Fig. 4.7 A). For a frequency $\omega/(2\pi) \sim 2$ GHz, $k_0 \equiv \omega/c = 4.19$ rad/m with characteristic wavelength $\lambda_0 = 2\pi/k_0 = 0.15$ m. The wavelength of the excited spin waves is much smaller than this scale, indicating that $\sqrt{k_y^2+k_z^2} \gg \omega/c$. Thus, $k_x \to i\sqrt{k_y^2+k_z^2} = i\kappa$. With $\kappa\delta \ll 1$:

$$\begin{aligned} H_x^{(i)}(x;k_y,k_z) &= -2iJ_i(\omega)e^{\kappa x}\frac{e^{-\kappa\delta}-1}{\kappa^2}\sin\left(k_y\frac{w}{2}\right)\frac{\sin(k_z l_i/2)}{k_z}e^{-ik_z z_i}, \\ H_y^{(i)}(x;k_y,k_z) &= 2J_i(\omega)e^{\kappa x}\frac{e^{-\kappa\delta}-1}{\kappa k_y}\sin\left(k_y\frac{w}{2}\right)\frac{\sin(k_z l_i/2)}{k_z}e^{-ik_z z_i}. \end{aligned} \tag{4.10}$$

The magnetic field distribution in $\mathbf{k}$-space is plotted in Fig. 4.7 A for the sample dimensions specified above, emphasizing the fast k_z oscillations. A microwave excitation with field components $h_x = \pm i h_y$ is circularly polarized. The relation

$$H_x(x;k_y,k_z) = -i(k_y/\kappa)H_y(x;k_y,k_z). \tag{4.11}$$

implies that when $|k_y| \ll |k_z|$, $|H_x| \ll |H_y|$, so the radiation is nearly linearly-polarized along the $\hat{\mathbf{y}}$-direction (in momentum space). On the other hand, when $|k_y| \gg |k_z|$, $H_x(x;k_y,k_z) \to$

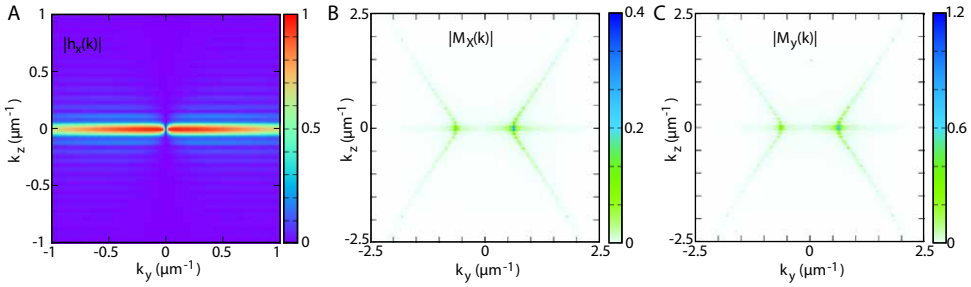

Figure 4.7: Drive field and excited magnetization in reciprocal space. **(A)** $x-$component of the magnetic field generated by the stripline in momentum space. **(B)-(C)** Resulting transverse magnetization amplitude, for $\alpha_G = 1\times10^{-4}$, $\omega = 2.29$ GHz, $\mu_0 M_s = 0.178$ T, and applied magnetic field $B_0 = 20$ mT. Note the different scales used for plotting $|M_x|$ and $|M_y|$.

$-i\mathrm{sgn}(k_y)H_y(x;k_y,k_z)$ is nearly right- (left-) circularly polarized for positive (negative) k_y. The polarization-momentum locking of the stripline magnetic field is responsible for the chiral pumping of circularly-polarized spin waves [24, 30, 47].

Excited magnetization

The stripline magnetic field excites spin waves in the YIG film. In the mixed position and momentum space, the dynamic magnetization $\mathbf{M}(x,\mathbf{k},\omega)$ reads in linear response [24, 30, 47]

$$M_\alpha(x,\mathbf{k},\omega) = \frac{1}{d}\int_{-d}^{0} dx'\,\chi_{\alpha\beta}(x,x',\mathbf{k},\omega)H_\beta(x',\mathbf{k},\omega) \tag{4.12}$$

where we sum over repeated Cartesian indices $\alpha,\beta = \{x,y,z\}$. γ is the electron gyromagnetic ratio and the spin susceptibility reads [24]

$$\chi_{\alpha\beta}(x,x',\mathbf{k},\omega) = -\gamma\mu_0 M_s m_\alpha^{\mathbf{k}}(x)m_\beta^{\mathbf{k}*}(x')\frac{1}{\omega-\omega_{\mathbf{k}}+i\Gamma_{\mathbf{k}}}. \tag{4.13}$$

Here, $m_\alpha^{\mathbf{k}}(x)$ characterize the ellipticity of the magnetization precession associated with the spin waves (see Eq. (4.15) and Eq. (4.17)), and $\Gamma_{\mathbf{k}} = 2\alpha_G\omega_{\mathbf{k}}$ is the Gilbert damping of the spin waves with frequency $\omega_{\mathbf{k}}$.

For the parameters of our experiments, the spin waves are in the dipolar-exchange regime with strongly anisotropic dispersion. For the long wavelengths considered here, the magnetization is homogeneous across the film thickness, which allows for an analytical treatment. The spin-wave dispersion for free magnetization boundary conditions reads [24, 30, 47]

$$\omega_{\mathbf{k}} = \gamma\mu_0 M_s\sqrt{\left[\Omega_H+\alpha_{\mathrm{ex}}k^2+1-f(|k_y|)\right]\left[\Omega_H+\alpha_{\mathrm{ex}}k^2+(k_y^2/k^2)f(|k_y|)\right]}, \tag{4.14}$$

where α_{ex} is the exchange stiffness, $\Omega_H \equiv B_0 \cos(\phi)/\mu_0 M_s$, and

$$f(|k_y|) = 1 - \frac{1}{|k_y|d} + \frac{1}{|k_y|d}\exp(-|k_y|d).$$

At long wavelengths, m_x and m_y are homogeneous across the film thickness and given by

$$m_x = \sqrt{\frac{\mathscr{D}+1}{(\mathscr{D}-1)}}, \quad m_y = i\sqrt{\frac{\mathscr{D}-1}{(\mathscr{D}+1)}}, \tag{4.15}$$

with

$$\mathscr{D} = \frac{1/2 - (1/2)\left(1 + k_y^2/k^2\right) f(|k_y|)}{\omega_{\mathbf{k}}/(\mu_0\gamma M_s) - \left(\Omega_H + \alpha_{\text{ex}}k_y^2 + 1/2\right) + (1/2)\left(1 - k_y^2/k^2\right) f(|k_y|)}. \tag{4.16}$$

We define the ellipticity parameter

$$\eta = \frac{|m_x|}{|m_y|} = \frac{\mathscr{D}+1}{\mathscr{D}-1}. \tag{4.17}$$

In the dipolar regime, the spin waves precess elliptically. When $\mathbf{k} \to 0$, $f(|k_y|) \to 0$, $\omega_{\mathbf{k}} \to \mu_0\gamma M_s\sqrt{\Omega_H(\Omega_H+1)}$ (corresponding to the FMR frequency), $\mathscr{D} \to -1-2\Omega_H-2\sqrt{\Omega_H(\Omega_H+1)}$. When $\Omega_H \to 0$ with a small static magnetic field, $\mathscr{D} \to -1-2\sqrt{\Omega_H}$, $|m_y| \gg |m_x|$, leading to a (nearly) linearly-polarized Kittel mode. When k is large, the exchange interaction dominates and the spin waves are right-circularly polarized.

We plot the calculated excited transverse magnetization amplitude in momentum space in Fig. 4.7B-C with parameters similar to those in Fig. 4F of the main text, i.e. $M_s = 1.42 \cdot 10^5$ A/m, $\alpha_G = 1 \times 10^{-4}$, $\omega/2\pi = 2.29$ GHz. The momentum distribution of the resonantly excited spin waves reflects the hyperboles formed by the cut through the anisotropic spin wave dispersion at the given frequency. The excitation becomes unidirectional when the spin waves are circularly-polarized [24, 47], in which case only those with positive values of k_y are excited. Due to the YIG thickness much smaller than the wavelengths considered, this chirality is not the intrinsic one of Damon-Eshbach surface modes, which exist only in much thicker films

The real part of the inverse Fourier transform of Eq. (4.12) gives the observable spatiotemporal magnetization

$$\mathbf{M}_\alpha(\boldsymbol{\rho}, t) = \frac{1}{4\pi^2}\iint d\mathbf{k} e^{i\boldsymbol{\rho}\cdot\mathbf{k} - i\omega t}\mathbf{M}_\alpha(x, \mathbf{k}) \tag{4.18}$$

with $\boldsymbol{\rho} = (y, z)$. Using this equation, we calculate a snapshot of the dynamic magnetization when spin waves are driven by a stripline as in Fig. 4 of the main text (Fig. 4.8). We observe interference of spin waves with frequency ω. Triangular areas of weak and strong excitation exist at the sides and in front of the stripline, respectively, with a spin wave focus point at the vertex of the latter triangle. These features can be understood from the anisotropy of the spin wave dispersion that leads to a critical opening angle of available spin wave momenta at a given frequency.

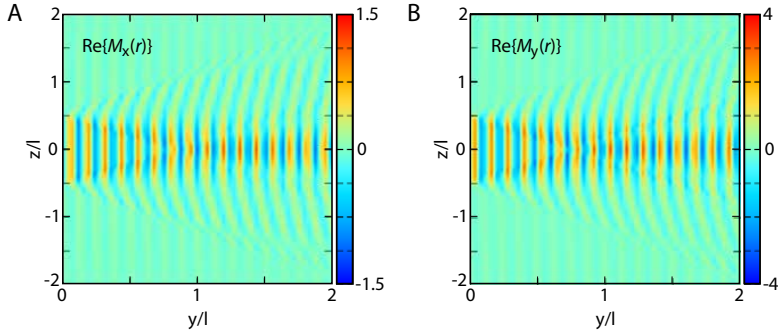

Figure 4.8: Spatial profile of the excited magnetization. Spatial profile of the out-of-plane (A) and in-plane **(B)** of the transverse magnetization oscillations excited by a single stripline, located at $y = 0$ between $z/l = -0.5$ and $z/l = +0.5$.

DIPOLAR FIELD AND RABI FREQUENCY

When the frequency of the magnetic stray field generated by a spin wave matches an NV ESR frequency, it can drive Rabi rotations of the NV spin if it has a circularly polarized component of the correct handedness. Here we describe the spin-wave induced Rabi driving of the NV spins.

Dipolar field generated by an oscillating magnetization

The magnetic field generated by a magnetization pattern can be calculated using Coulomb's law [45]

$$\mathbf{B}_\beta(\mathbf{r},t) = \frac{\mu_0}{4\pi}\partial_\beta\partial_\alpha \int d\mathbf{r}' \frac{\mathbf{M}_\alpha(\mathbf{r}',t)}{|\mathbf{r}-\mathbf{r}'|}. \tag{4.19}$$

By substituting the magnetization from Eq. (4.18) and using the Coulomb integral

$$\int d\mathbf{r}' \frac{e^{i\mathbf{k}\cdot\boldsymbol{\rho}'} f(x')}{|\mathbf{r}-\mathbf{r}'|} = \frac{2\pi}{k} e^{i\mathbf{k}\cdot\boldsymbol{\rho}} \int dx' e^{-|x-x'|k} f(x'), \tag{4.20}$$

where $k = |\mathbf{k}|$, we obtain the magnetic field above the film ($x > 0$) [24, 30, 47]

$$B_{SW,x}(x,\mathbf{k},t) = \frac{\mu_0}{2} e^{-kx-i\omega t}(1-e^{-kd})\left(M_x(\mathbf{k}) - i\frac{k_y}{k}M_y(\mathbf{k})\right), \tag{4.21}$$

with $B_{SW,y}(\mathbf{k}) = -i(k_y/k)B_{SW,x}(\mathbf{k})$, and $B_{SW,z}(\mathbf{k}) = -i(k_z/k)B_{SW,x}(\mathbf{k})$. Thus, when $|k_z| \ll |k_y|$, $B_{SW,y}(\mathbf{k}) = -i\,\mathrm{sign}(k_y)B_{SW,x}(\mathbf{k})$, i.e. the polarization and momentum are locked. $B_{SW,(x,y)}$ vanishes for negative k_y when the spin waves are right circularly-polarized since $M_x(\mathbf{k}) - iM_y(\mathbf{k})k_y/k \to 0$ [24, 47]. The right-forward dipolar field is left-circularly polarized.

In real space, the stray field generated by the spin wave is given by the real part of the inverse Fourier transform

$$\mathbf{B}_{SW}(x,\boldsymbol{\rho},t) = \frac{1}{4\pi^2}\iint e^{i\boldsymbol{\rho}\cdot\mathbf{k}}\mathbf{B}_{SW}(x,\mathbf{k},t)d\mathbf{k}. \tag{4.22}$$

A snapshot of the spin-wave stray field at a distance x_0 above the film is plotted in Fig. 4.9. Since the distance to the film is much smaller than the relevant wavelengths, the interference pattern of the spin waves is well resolved. We note that $|B_{SW,z}| \ll |B_{SW,x}|, |B_{SW,y}|$ because the excited spin waves propagate almost perpendicular to the stripline. The strong chirality (unidirectionality) is caused by both the stripline magnetic field (see in Fig. 4.7) and the stray field from the spin waves [24, 30, 47]. All Cartesian vector components exert a torque on the NV center spin, which is oriented at an angle to the film. The dipolar field shows a focal point with large amplitude, which can be controlled by tuning the magnetic field and stripline frequency, which could be interesting for spintronic applications.

The field of a spin wave that is characterized by $|k_z| \ll |k_y|$ (therefore $\mathbf{k} \perp \mathbf{M}$, corresponding to a Damon-Eshbach geometry and an effectively one-dimensional configuration) is given by ($x > 0$)

$$\mathbf{B}_{SW}(x,\mathbf{k},t) = -\frac{\mu_0}{2} e^{-kx-i\omega t}(1-e^{-kd}) M_y(\mathbf{k}) \left(1+\text{sign}(k_y)\eta\right)\left(\hat{\mathbf{y}} + i\,\text{sign}(k_y)\hat{\mathbf{x}}\right), \tag{4.23}$$

where we used $M_x = -i\eta M_y$. To arrive at the equations given in the main text, we calculate the field of a traveling spin wave given by the real part of $\mathbf{m}_\perp = m_\perp^0 e^{i(k_0 y-\omega t)}(\hat{\mathbf{y}} - i\eta\hat{\mathbf{x}})$. The Fourier transform of the y-component is

$$M_y(k_y) = m_\perp^0 2\pi\delta(k_y - k_0). \tag{4.24}$$

Substituting into Eq. (4.23) and taking the inverse Fourier transform, we get Eq.(4.2) of the main text

$$\mathbf{B}_{\text{SW}}(y) = -\text{Re}[\frac{\mu_0 m_\perp^0}{2} e^{-|k_0|x_0} e^{i(k_0 y-\omega t)}(1-e^{-|k_0|d})(1+\text{sign}(k_0)\eta)(\hat{\mathbf{y}} + i\,\text{sign}(k_0)\hat{\mathbf{x}})] \tag{4.25}$$

$$= -\text{Re}[B_{SW}^0 e^{i(k_0 y-\omega t)}(\hat{\mathbf{y}} + i\,\text{sign}(k_0)\hat{\mathbf{x}})] \tag{4.26}$$

Calculation of the Rabi frequency

The dynamic magnetic field generated by the spin waves can induce transitions between the spin states of the NV center when its frequency matches an NV ESR frequency as described by the NV spin Hamiltonian. We write the dynamic part of the magnetic field as

$$\mathbf{B}_{\text{SW}}(y) = \text{Re}[(B_x\hat{\mathbf{x}} + B_y\hat{\mathbf{y}} + B_z\hat{\mathbf{z}})e^{-i\omega t}] \tag{4.27}$$

In the local coordinates of the NV center, with the z'-direction along the applied static magnetic field (therefore along the NV axis), the field amplitudes becomes

$$B_{x'} = B_x\cos\phi - B_z\sin\phi, \tag{4.28}$$

$$B_{y'} = B_y, \tag{4.29}$$

$$B_{z'} = B_z\cos\phi + B_x\sin\phi. \tag{4.30}$$

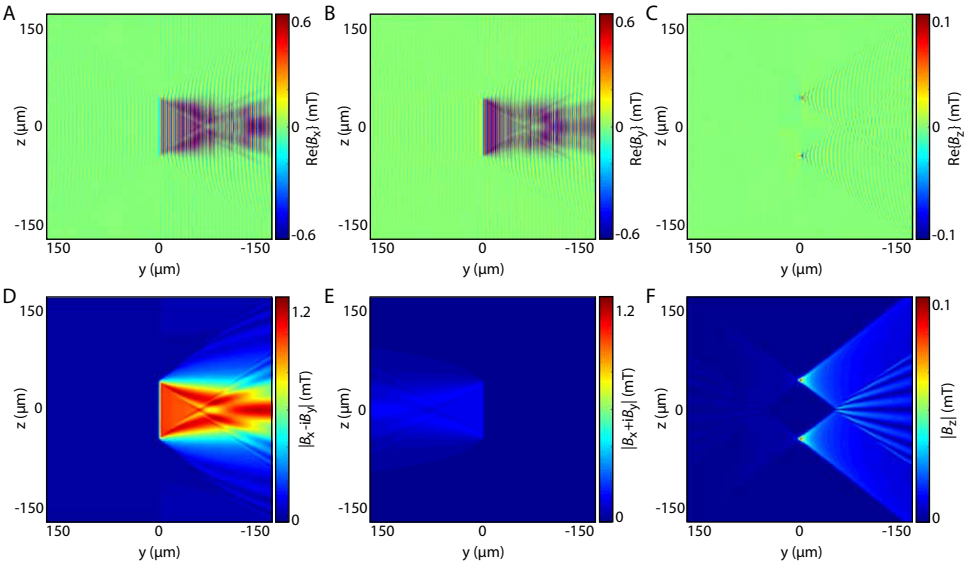

Figure 4.9: Spatial profile of the dipolar field generated by spin waves. Snapshot of the stray field in real space at $t = 0$ for a microwave driving with a frequency $\omega = 2.29$ GHz and a stripline current of 0.7 mA at a distance x_0 above the film. The stripline is located at $y = 0$, $z \in [-40, 40]$ μm. The damping coefficient is $\alpha_G = 10^{-4}$.

The Hamiltonian describing the NV spin dynamics is given by

$$H_{\mathrm{NV}} = DS_z^2 + \gamma \mathbf{B}' \cdot \mathbf{S} \tag{4.31}$$

where $\mathbf{S} = (S_x, S_y, S_z)$ are the Pauli matrices for a spin 1 and $D/2\pi = 2.87$ GHz is the zero-field frequency. The two magnetic-dipole allowed transitions between the $m_s = 0$ and the $m_s = \pm 1$ states are driven by magnetic fields of opposite handedness. When the magnetic-field frequency ω matches one of the NV ESR frequencies $D \pm \gamma B_0$, the NV spin will Rabi oscillate between the corresponding $m_s = 0$ and $m_s = \pm 1$ states with a Rabi frequency given by

$$\omega_R^{\pm} = \frac{\gamma}{\sqrt{2}} \left| B_{x'} \pm i B_{y'} \right|. \tag{4.32}$$

We use Eq. (4.32) to calculate the spin-wave induced Rabi frequency caused by the spatial magnetization profile shown in Fig. 4.8. The Rabi frequency closely resembles the spatial magnetization profile, including the presence of caustic beams and a focal point (Fig. 4.10).

When the NV ω_- transition is driven by a resonant Damon-Eshbach spin wave with $k_0 > 0$, we get

$$\omega_R^- = \sqrt{2}\gamma B_{\mathrm{SW}}^0 \cos^2 \frac{\phi}{2}. \tag{4.33}$$

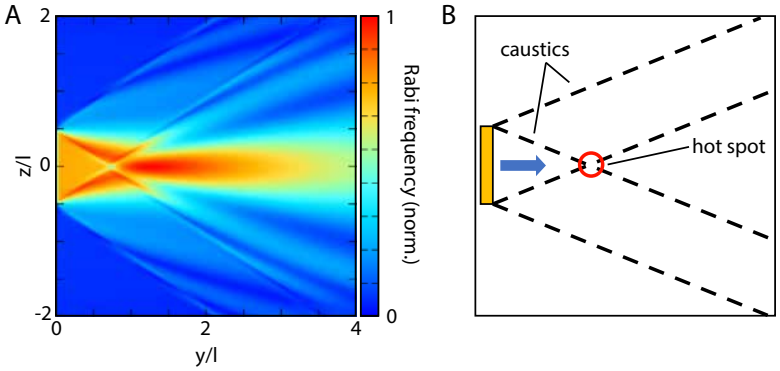

Figure 4.10: Calculated spatial map of the Rabi frequency for a single stripline. **(A)** Rabi frequency calculated from the dipolar field without the (small) direct contribution from the stripline at $y = 0$ and $z/l \in [-0.5, 0.5]$. **(B)** Schematics indicating the emergence of caustic spin-wave beams and the "hot spot" where energy gets focussed.

If the NV spin is also driven by a magnetic field that is given by $\mathrm{Re}[\mathbf{B}_{\mathrm{REF}} e^{-i\omega t}]$, we get

$$\omega_R^- = \frac{\gamma}{\sqrt{2}} \left| 2B_{\mathrm{SW}}^0 e^{ik_0 y} \cos^2 \frac{\phi}{2} + B_{\mathrm{REF,x'}} - iB_{\mathrm{REF,y'}} \right|. \tag{4.34}$$

from which follows Eq. 4.3 of the main text. Including a damping parameter into Eq. (4.34), we fit the data of Fig. 2B of the main text, from which we extract the spin-wave amplitude $m_\perp^0$ (using the ellipticity parameter calculated with Eq. (4.17)) and the spin-wave damping:

$$\omega_R^- = \frac{\gamma}{\sqrt{2}} \left| 2B_{\mathrm{SW}}^0 e^{ik_0 y - y/y_0} \cos^2 \frac{\phi}{2} + e^{i\theta} B_{\mathrm{REF}} \right|. \tag{4.35}$$

Here, y_0 is the spin-wave decay length from which the Gilbert damping parameter is extracted using $y_0 = v_g/(2\omega\alpha_G)$, with v_g the group velocity, leading to $\alpha_G = 1.2(1) \cdot 10^{-4}$. The main contribution to the uncertainty is caused by the uncertainty in the NV-YIG distance, which we measured to be 1.8(2) µm (see section 4.5.1) at the location of the stripline and which increases by about 0.4 µm/mm as estimated from the optical interference fringes visible in Fig. 1B of the main text (the distance change between two fringes is given by $\lambda_0/2$, with λ_0 the wavelength of the light in air). Using Eq. (4.35), we also fitted the data shown in Fig. 3B of the main text, with B_{REF} given by Eq. (4.5).

EFFECT OF MAGNETIC FIELD MISALIGNMENT ON THE OBSERVED SPIN-WAVE PATTERNS

To explain the asymmetry along $\hat{\mathbf{z}}$ of the observed spin-wave patterns in Fig. 4, we repeat the calculation of Fig. 4C with the introduction of a 5° misalignment between the static field and the stripline (Fig. 4.11). The tilt is from the $\hat{\mathbf{z}}$ toward the $-\hat{\mathbf{y}}$ axis.

INFLUENCE OF THE SPIN-WAVE PROPAGATION DIRECTION ON THE FIELD PROFILE

As previously explained (Eq. (4.32)), right(left)-propagating spin waves generate a circularly-polarized field with handedness that drives the ω_- (ω_+) transition. Moreover, for perfectly circular polarization, the right(left)-propagating waves only generate a field above

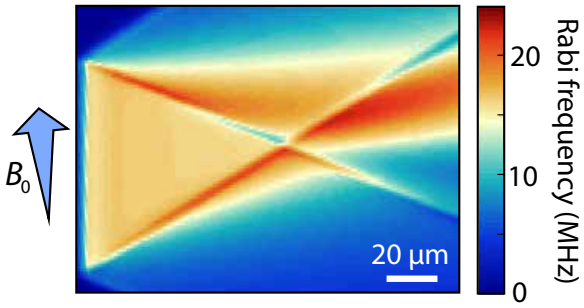

Figure 4.11: Effect of a small angle between the stripline and the in-plane component of the static field $\mathbf{B_0}$. Calculated spatial map of the Rabi frequency when the in-plane projection of the static field (B_0) is oriented at a 5° angle from the stripline.

(below) the film, which can be simply explained by cancellation of the field contributions of neighbouring spins (Fig. 4.12). For elliptical polarization, the field suppression is not complete.

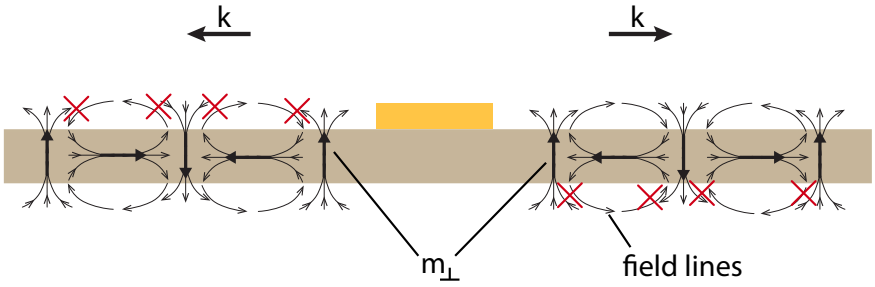

Figure 4.12: Magnetic field generated by spin waves propagating to the left and right. The magnetic stray field generated by a spin wave is the sum of the fields generated by the individual precessing spins in the magnet. The phases of the spin waves traveling to the right interfere constructively/destructively above/below the film, and vice versa for spin waves traveling to the left.

INTERFERENCE BETWEEN SPIN WAVES GENERATED BY TWO ADJACENT STRIPLINES

Finally, we calculate the interference pattern generated by two striplines on the YIG film, with centers separated by 200 µm. With $l_1 = 100$ µm and $l_2 = -100$ µm in Eq. (4.10) and considering the π phase difference between the two striplines

$$H_x(x;k_y,k_z) = -2iJ(\omega)e^{\kappa x}\frac{e^{-\kappa\delta}-1}{\kappa^2}\sin\left(k_y\frac{w}{2}\right)\frac{\sin(k_z l/2)}{k_z}(e^{-ik_z z_1}-e^{-ik_z z_2}), \tag{4.36}$$

$$H_y(x;k_y,k_z) = 2J(\omega)e^{\kappa x}\frac{e^{-\kappa\delta}-1}{\kappa k_y}\sin\left(k_y\frac{w}{2}\right)\frac{\sin(k_z l/2)}{k_z}(e^{-ik_z z_1}-e^{-ik_z z_2}). \tag{4.37}$$

By substitution into Eqs. (4.12) and (4.21), we obtain the Rabi frequencies of the NV center in Figure 4.13. The spin-wave interference is clearly reflected in the Rabi frequency.

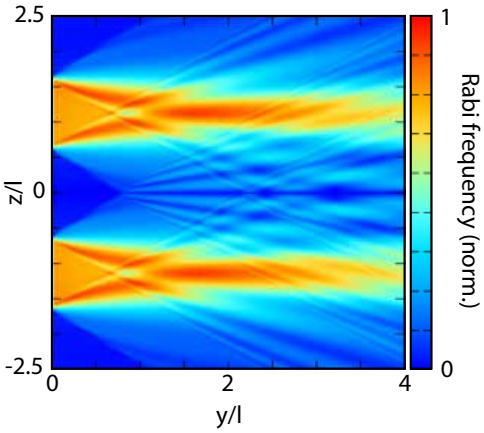

Figure 4.13: Calculated spatial map of the Rabi frequency induced by two adjacent striplines. We observe interference of spin waves generated by two striplines located at $y = 0$ for $z \in \pm[0.5, 1.5]$.

REFERENCES

[1] V. V. Kruglyak, S. O. Demokritov, and D. Grundler, *Magnonics,* Journal of Physics D: Applied Physics **43**, 264001 (2010).

[2] A. V. Chumak, V. I. Vasyuchka, A. A. Serga, and B. Hillebrands, *Magnon spintronics,* Nature Physics **11**, 453 (2015).

[3] K. Vogt, F. Y. Fradin, J. E. Pearson, T. Sebastian, S. D. Bader, B. Hillebrands, A. Hoffmann, and H. Schultheiss, *Realization of a spin-wave multiplexer,* Nature Communications **5**, 3727 (2014).

[4] A. V. Chumak, A. A. Serga, and B. Hillebrands, *Magnon transistor for all-magnon data processing,* Nature Communications **5**, 4700 (2014).

[5] L. J. Cornelissen, J. Liu, B. J. van Wees, and R. A. Duine, *Spin-Current-Controlled Modulation of the Magnon Spin Conductance in a Three-Terminal Magnon Transistor,* Physical Review Letters **120**, 097702 (2018).

[6] V. E. Demidov, H. Ulrichs, S. V. Gurevich, S. O. Demokritov, V. S. Tiberkevich, A. N. Slavin, A. Zholud, and S. Urazhdin, *Synchronization of spin Hall nano-oscillators to external microwave signals.* Nature communications **5**, 3179 (2014).

[7] Q. Wang, P. Pirro, R. Verba, A. Slavin, B. Hillebrands, and A. V. Chumak, *Reconfigurable nanoscale spin-wave directional coupler,* Science Advances **4**, e1701517 (2018).

[8] T. Warwick, K. Franck, J. B. Kortright, G. Meigs, M. Moronne, S. Myneni, E. Rotenberg, S. Seal, W. F. Steele, H. Ade, A. Garcia, S. Cerasari, J. Denlinger, S. Hayakawa, A. P. Hitchcock, T. Tyliszczak, J. Kikuma, E. G. Rightor, H. J. Shin, and B. P. Tonner, *A scanning transmission x-ray microscope for materials science spectromicroscopy at the advanced light source,* Review of Scientific Instruments **69**, 2964 (1998).

[9] V. Sluka, T. Schneider, R. A. Gallardo, A. Kákay, M. Weigand, T. Warnatz, R. Mattheis, A. Roldán-Molina, P. Landeros, V. Tiberkevich, A. Slavin, G. Schütz, A. Erbe, A. Deac, J. Lindner, J. Raabe, J. Fassbender, and S. Wintz, *Emission and propagation of 1D and 2D spin waves with nanoscale wavelengths in anisotropic spin textures,* Nature Nanotechnology **14**, 328 (2019).

[10] T. Sebastian, K. Schultheiss, B. Obry, B. Hillebrands, and H. Schultheiss, *Micro-focused Brillouin light scattering: imaging spin waves at the nanoscale,* Frontiers in Physics **3**, 35 (2015).

[11] Y. Acremann, C. H. Back, M. Buess, O. Portmann, A. Vaterlaus, D. Pescia, and H. Melchior, *Imaging precessional motion of the magnetization vector,* Science **290**, 492 (2000).

[12] L. Rondin, J. P. Tetienne, T. Hingant, J. F. Roch, P. Maletinsky, and V. Jacques, *Magnetometry with nitrogen-vacancy defects in diamond,* Reports on Progress in Physics **77**, 056503 (2014).

[13] F. Casola, T. van der Sar, and A. Yacoby, *Probing condensed matter physics with magnetometry based on nitrogen-vacancy centres in diamond,* Nature Reviews Materials **3**, 17088 (2018).

[14] I. Gross, W. Akhtar, V. Garcia, L. J. Martínez, S. Chouaieb, K. Garcia, C. Carrétéro, A. Barthélémy, P. Appel, P. Maletinsky, J. V. Kim, J. Y. Chauleau, N. Jaouen, M. Viret, M. Bibes, S. Fusil, and V. Jacques, *Real-space imaging of non-collinear antiferromagnetic order with a single-spin magnetometer,* Nature **549**, 252 (2017).

[15] L. Rondin, J.-P. Tetienne, S. Rohart, A. Thiaville, T. Hingant, P. Spinicelli, J.-F. Roch, and V. Jacques, *Stray-field imaging of magnetic vortices with a single diamond spin.* Nature communications **4**, 2279 (2013).

[16] Y. Dovzhenko, F. Casola, S. Schlotter, T. X. Zhou, F. Büttner, R. L. Walsworth, G. S. Beach, and A. Yacoby, *Magnetostatic twists in room-temperature skyrmions explored by nitrogen-vacancy center spin texture reconstruction,* Nature Communications **9**, 2712 (2018).

[17] T. van der Sar, F. Casola, R. Walsworth, and A. Yacoby, *Nanometre-scale probing of spin waves using single-electron spins.* Nature communications **6**, 7886 (2015).

[18] C. Du, T. van der Sar, T. X. Zhou, P. Upadhyaya, F. Casola, H. Zhang, M. C. Onbasli, C. A. Ross, R. L. Walsworth, Y. Tserkovnyak, and A. Yacoby, *Control and local measurement of the spin chemical potential in a magnetic insulator,* Science **357**, 195 (2017).

[19] P. Andrich, C. F. de las Casas, X. Liu, H. L. Bretscher, J. R. Berman, F. J. Heremans, P. F. Nealey, and D. D. Awschalom, *Long-range spin wave mediated control of defect qubits in nanodiamonds,* npj Quantum Information **3**, 28 (2017).

[20] D. Kikuchi, D. Prananto, K. Hayashi, A. Laraoui, N. Mizuochi, M. Hatano, E. Saitoh, Y. Kim, C. A. Meriles, and T. An, *Long-distance excitation of nitrogen-vacancy centers in diamond via surface spin waves,* Applied Physics Express **10**, 103004 (2017).

[21] C. S. Wolfe, V. P. Bhallamudi, H. L. Wang, C. H. Du, S. Manuilov, R. M. Teeling-Smith, a. J. Berger, R. Adur, F. Y. Yang, and P. C. Hammel, *Off-resonant manipulation of spins in diamond via precessing magnetization of a proximal ferromagnet,* Physical Review B **89**, 180406 (2014).

[22] L. Thiel, Z. Wang, M. A. Tschudin, D. Rohner, I. Gutiérrez-Lezama, N. Ubrig, M. Gibertini, E. Giannini, A. F. Morpurgo, and P. Maletinsky, *Probing magnetism in 2D materials at the nanoscale with single-spin microscopy,* Science **364**, 973 (2019).

[23] A. A. Serga, A. V. Chumak, and B. Hillebrands, *YIG magnonics,* Journal of Physics D: Applied Physics **43**, 264002 (2010).

[24] T. Yu, Y. M. Blanter, and G. E. W. Bauer, *Chiral Pumping of Spin Waves,* Physical Review Letters **123**, 247202 (2019).

[25] C. Dubs, O. Surzhenko, R. Linke, A. Danilewsky, U. Brückner, and J. Dellith, *Sub-micrometer yttrium iron garnet LPE films with low ferromagnetic resonance losses,* Journal of Physics D: Applied Physics **50**, 204005 (2017).

[26] T. Schneider, A. A. Serga, A. V. Chumak, C. W. Sandweg, S. Trudel, S. Wolff, M. P. Kostylev, V. S. Tiberkevich, A. N. Slavin, and B. Hillebrands, *Nondiffractive subwavelength wave beams in a medium with externally controlled anisotropy,* Physical Review Letters **104**, 197203 (2010).

[27] R. Gieniusz, H. Ulrichs, V. D. Bessonov, U. Guzowska, A. I. Stognii, and A. Maziewski, *Single antidot as a passive way to create caustic spin-wave beams in yttrium iron garnet films,* Applied Physics Letters **102**, 102409 (2013).

[28] M. Mohseni, R. Verba, T. Brächer, Q. Wang, D. A. Bozhko, B. Hillebrands, and P. Pirro, *Backscattering Immunity of Dipole-Exchange Magnetostatic Surface Spin Waves,* Physical Review Letters **122**, 197201 (2019).

[29] J. R. Eshbach and R. W. Damon, *Surface magnetostatic modes and surface spin waves,* Physical Review **118**, 1208 (1960).

[30] J. Chen, T. Yu, C. Liu, T. Liu, M. Madami, K. Shen, J. Zhang, S. Tu, M. S. Alam, K. Xia, M. Wu, G. Gubbiotti, Y. M. Blanter, G. E. W. Bauer, and H. Yu, *Excitation of unidirectional exchange spin waves by a nanoscale magnetic grating,* Physical Review B **100**, 104427 (2019).

[31] J. P. Tetienne, N. Dontschuk, D. A. Broadway, A. Stacey, D. A. Simpson, and L. C. Hollenberg, *Quantum imaging of current flow in graphene,* Science Advances **3**, e1602429 (2017).

[32] T. Rosskopf, A. Dussaux, K. Ohashi, M. Loretz, R. Schirhagl, H. Watanabe, S. Shikata, K. M. Itoh, and C. L. Degen, *Investigation of surface magnetic noise by shallow spins in diamond,* Physical Review Letters **112**, 147602 (2014).

[33] C. Wei, A. S. Windsor, and N. B. Manson, *A strongly driven two-level atom revisited: Bloch-Siegert shift versus dynamic Stark splitting,* Journal of Physics B: Atomic, Molecular and Optical Physics **30**, 21 (1997).

[34] B. Flebus and Y. Tserkovnyak, *Quantum-Impurity Relaxometry of Magnetization Dynamics,* Physical Review Letters **121**, 187204 (2018).

[35] K. Arai, C. Belthangady, H. Zhang, N. Bar-Gill, S. J. Devience, P. Cappellaro, A. Yada, and R. L. Walsworth, *Fourier magnetic imaging with nanoscale resolution and compressed sensing speed-up using electronic spins in diamond,* Nature Nanotechnology **10**, 859 (2015).

[36] G. Balasubramanian, I. Y. Chan, R. Kolesov, M. Al-Hmoud, J. Tisler, C. Shin, C. Kim, A. Wojcik, P. R. Hemmer, A. Krueger, T. Hanke, A. Leitenstorfer, R. Bratschitsch, F. Jelezko, and J. Wrachtrup, *Nanoscale imaging magnetometry with diamond spins under ambient conditions,* Nature **455**, 648 (2008).

[37] L. Thiel, D. Rohner, M. Ganzhorn, P. Appel, E. Neu, B. Müller, R. Kleiner, D. Koelle, and P. Maletinsky, *Quantitative nanoscale vortex imaging using a cryogenic quantum magnetometer,* Nature Nanotechnology **11**, 677 (2016).

[38] M. Pelliccione, A. Jenkins, P. Ovartchaiyapong, C. Reetz, E. Emmanouilidou, N. Ni, and A. C. Bleszynski Jayich, *Scanned probe imaging of nanoscale magnetism at cryogenic temperatures with a single-spin quantum sensor,* Nature Nanotechnology **11**, 700 (2016).

[39] E. Schaefer-Nolte, F. Reinhard, M. Ternes, J. Wrachtrup, and K. Kern, *A diamond-based scanning probe spin sensor operating at low temperature in ultra-high vacuum,* Review of Scientific Instruments **85**, 013701 (2014).

[40] J. M. Cai, B. Naydenov, R. Pfeiffer, L. P. McGuinness, K. D. Jahnke, F. Jelezko, M. B. Plenio, and A. Retzker, *Robust dynamical decoupling with concatenated continuous driving,* New Journal of Physics **14**, 113023 (2012).

[41] S. E. Lillie, N. Dontschuk, D. A. Broadway, D. L. Creedon, L. C. Hollenberg, and J. P. Tetienne, *Imaging Graphene Field-Effect Transistors on Diamond Using Nitrogen-Vacancy Microscopy,* Physical Review Applied **12**, 024018 (2019).

[42] S. Bogdanović, M. S. Liddy, S. B. Van Dam, L. C. Coenen, T. Fink, M. Lončar, and R. Hanson, *Robust nano-fabrication of an integrated platform for spin control in a tunable microcavity,* APL Photonics **2**, 126101 (2017).

[43] M. A. Schoen, J. M. Shaw, H. T. Nembach, M. Weiler, and T. J. Silva, *Radiative damping in waveguide-based ferromagnetic resonance measured via analysis of perpendicular standing spin waves in sputtered permalloy films,* Physical Review B **92**, 184417 (2015).

[44] B. A. Kalinikos and A. N. Slavin, *Theory of dipole-exchange spin wave spectrum for ferromagnetic films with mixed exchange boundary conditions,* Journal of Physics C: Solid State Physics **19**, 7013 (1986).

[45] J. D. Jackson, *John wiley & sons* (Wiley, New York, 1998).

[46] L. Novotny and B. Hecht, *Principles of nano-optics* (Cambridge University Press, Cambridge, 2006).

[47] T. Yu, C. Liu, H. Yu, Y. M. Blanter, and G. E. Bauer, *Chiral excitation of spin waves in ferromagnetic films by magnetic nanowire gratings,* Physical Review B **99**, 134424 (2019).